

Electronic Supplementary Information†

Nanoengineering of the $\text{Cu}_2\text{ZnSnS}_4\text{-TiO}_2$ Interface *via* Atomic Layer Deposition of Al_2O_3 for High Sensitivity Photodetectors and Solid State Nanostructured Solar Cells

*Zhuoran Wang, Nicolas Brodusch, Raynald Gauvin, and George P. Demopoulos**

Materials Engineering, McGill University, 3610 University Street, Montreal, QC, Canada H3A 0C5

* george.demopoulos@mcgill.ca

Experimental Section

Material Synthesis

TiO_2 nanorod growth^{1,2}

To grow vertically aligned TiO_2 nanorods on FTO glass, a piece of pre-cleaned fluorine doped tin oxide (FTO) glass (Sigma-Aldrich, $7 \Omega/\text{sq}$) was placed with the conductive side facing downward in a 125 ml Teflon container. An acidic solution (20 mL) was poured into the container made of hydrochloric acid solution (6M) (18% by weight, Sigma-Aldrich) and 75mM Ti as titanium butoxide (97 %, Sigma-Aldrich). The whole container was then placed into a stainless steel autoclave and kept at 150°C for 2 hours. After the hydrothermal reaction, well aligned TiO_2 nanorod arrays were deposited on the FTO glass, which were subsequently subjected to thermal treatment-annealing at 500°C in air.

Deposition of CZTS

Subsequently spin coating was employed to deposit the CZTS precursor material containing Cu, Zn, Sn and S on the TiO₂ nanorod array using clear solution as we reported in a previous work.³ Specifically, 0.09M CuCl₂ (99%, Alfa Aesar), 0.06M ZnCl₂ (99.99%, Sigma-Aldrich), 0.07M SnCl₂ (98%, Sigma-Aldrich) and 0.4M thioacetamide were dissolved in 20 mL ethanol/water mixed solution ($V_{\text{ethanol}}: V_{\text{water}} = 3:1$) to form a clear yellowish solution. The prepared solution was spin-coated on TiO₂ nanorods/FTO substrate at 2,500 rpm for 20s. The film was pre-baked in Air at 250 °C for 5 min after each spin coating cycle. Finally the films were annealed (Mini CVD Tube Furnace, MTI Corporation) at 600 °C for 30 min and later at 580 °C in the presence of 50 mg S and 100 mg Sn powder to crystallize CZTS.

Atomic layer deposition of Al₂O₃

The Al₂O₃ was deposited on pure TiO₂ nanorods before the deposition of CZTS. Atomic layer deposition was performed with GEMStar-6XT using trimethylaluminum (TMA) and H₂O as precursor at 175 °C. The deposition rate on Si was estimated to be 0.1 nm/cycle.

Device fabrication

For solid state device, the hole-transporting material (HTM) was formed on the TNR-CZTS film by spin-coating the 2,2',7,7'-tetrakis(N,N-dimethoxyphenylamino)-9,9'-spirobifluorene (spiro-OMeTAD) solution at 2,500 rpm for 20 s, where 72.3 mg of spiro-OMeTAD was mixed with 28.8 μL of 4-tert-butylpyridine and 17.5 μL of lithium bis(trifluoromethylsulfonyl) imide (LiTFSI) solution (520 mg of LiTFSI in 1 mL of acetonitrile) in 1 mL of chlorobenzene. Finally, 80 nm of Au was deposited using a thermal evaporator at a deposition rate of 1.0 Å/s, a shadow mask was used to give active area of 0.13 cm² for all devices. CdS was prepared via chemical bath deposition (CBD)⁴ at 65 °C for 20 min on TiO₂ nanorod film before coating CZTS precursor.

Characterization Methods

Thermo Scientific K-Alpha X-Ray Photoelectron Spectroscopy (XPS) was used for surface analysis. (C 1s peak at binding energy of 285 eV was used for charge correction) Hitachi SU-8230 Field Emission-STEM (FE-STEM) with Oxford EBSD and INCA EDS was used for high resolution SEM secondary electron and backscatter electron images capturing and EDS mapping. X-ray absorption near-edgespectroscopy (XANES) was performed at the soft X-ray microcharacterization (SXRMB, 06B1-1) beamlines. The Ti and S K-edge XANES spectra were measured at the SXRMB beamline, which has an energy range of 1.7–10 keV and resolution of ~ 3000 . The powder and thin film samples were fixed by double-sided carbon tape on the sample plate and mounted 45° toward the incident X-ray beam. The TEY measures specimen current resulting from photoelectrons, Auger electrons, and secondary electrons. All spectra were normalized to incident photon flux (I_0). The reference samples of Cu_2S , SnS , ZnS were purchased from Sigma-Aldrich, SnS_2 and pure TNR were synthesized in lab and characterized by XRD, EDS and XPS to confirm their purity. An IPCE/EQE system from PVM Inc. was used for optical and EQE measurements. Newport AM1.5 solar simulator was used for J-V or I-V characteristic measurement. All solar cells were soaked into light at $100\text{mW}/\text{cm}^2$ for 1~3h before testing.

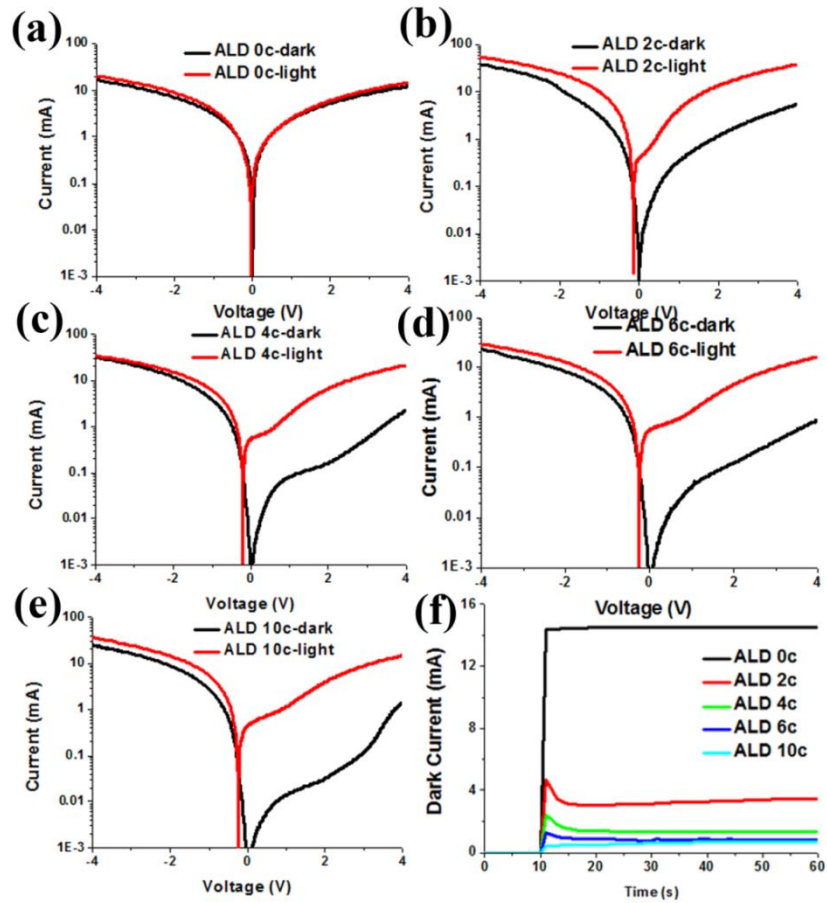


Fig. S1 a-e) I-V characteristics of photodiodes with variable number of ALD deposited Al_2O_3 layers and f) the dark current measured under 4 V reverse bias.

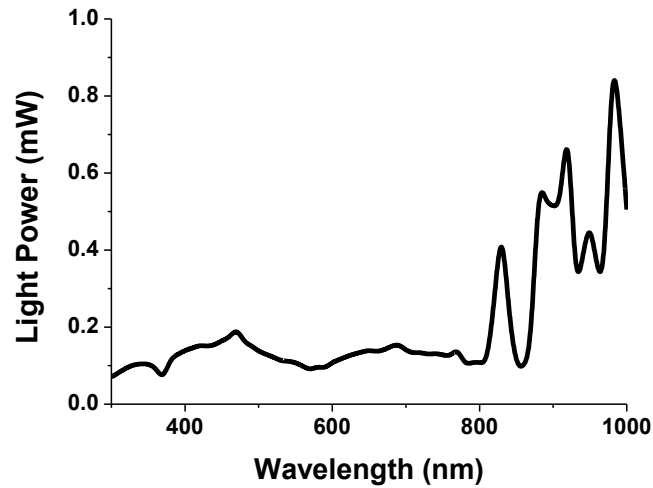


Fig. S2 Spectrum of the monochromatic light source used for responsivity and EQE measurement.

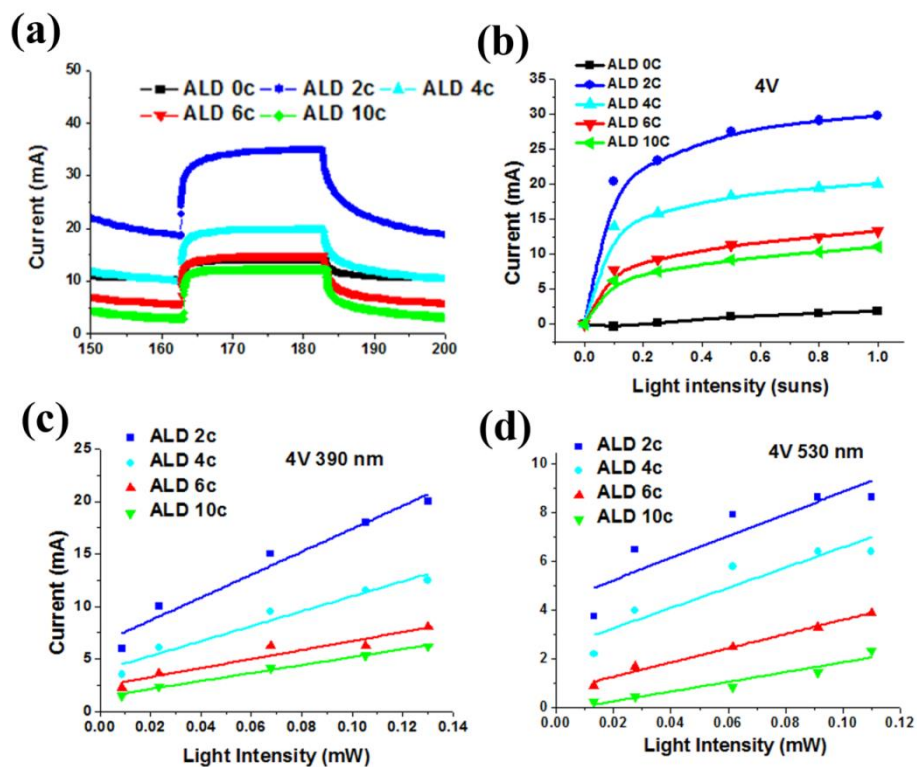


Fig. S3 (a) The optical switching property of the devices under 4V reversed bias with different layers of ALD deposited Al_2O_3 (magnified image of Fig. 1b) and their light intensity dependent photocurrent under (b) solar simulator and (c) 390 nm and d) 530 nm low power monochromatic light.

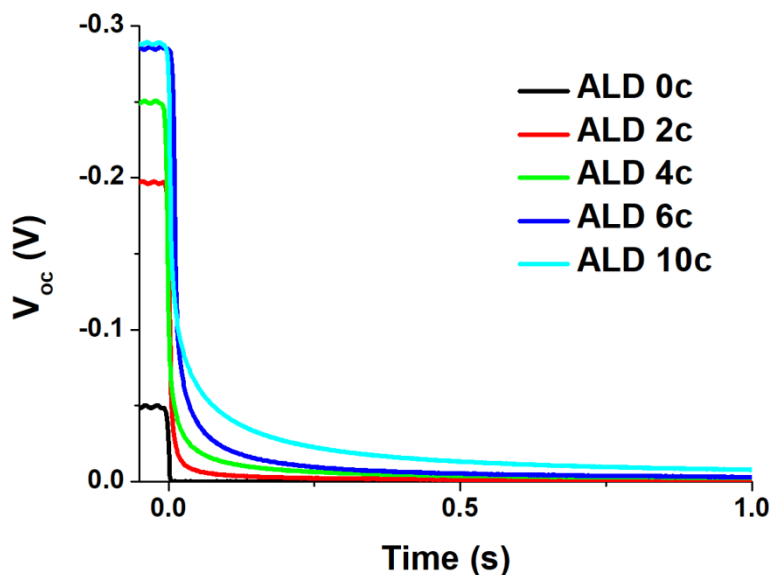


Fig. S4 Open-circuit voltage decay measurement after turning off the light for photovoltaic devices with different layers of ALD deposited Al_2O_3 .

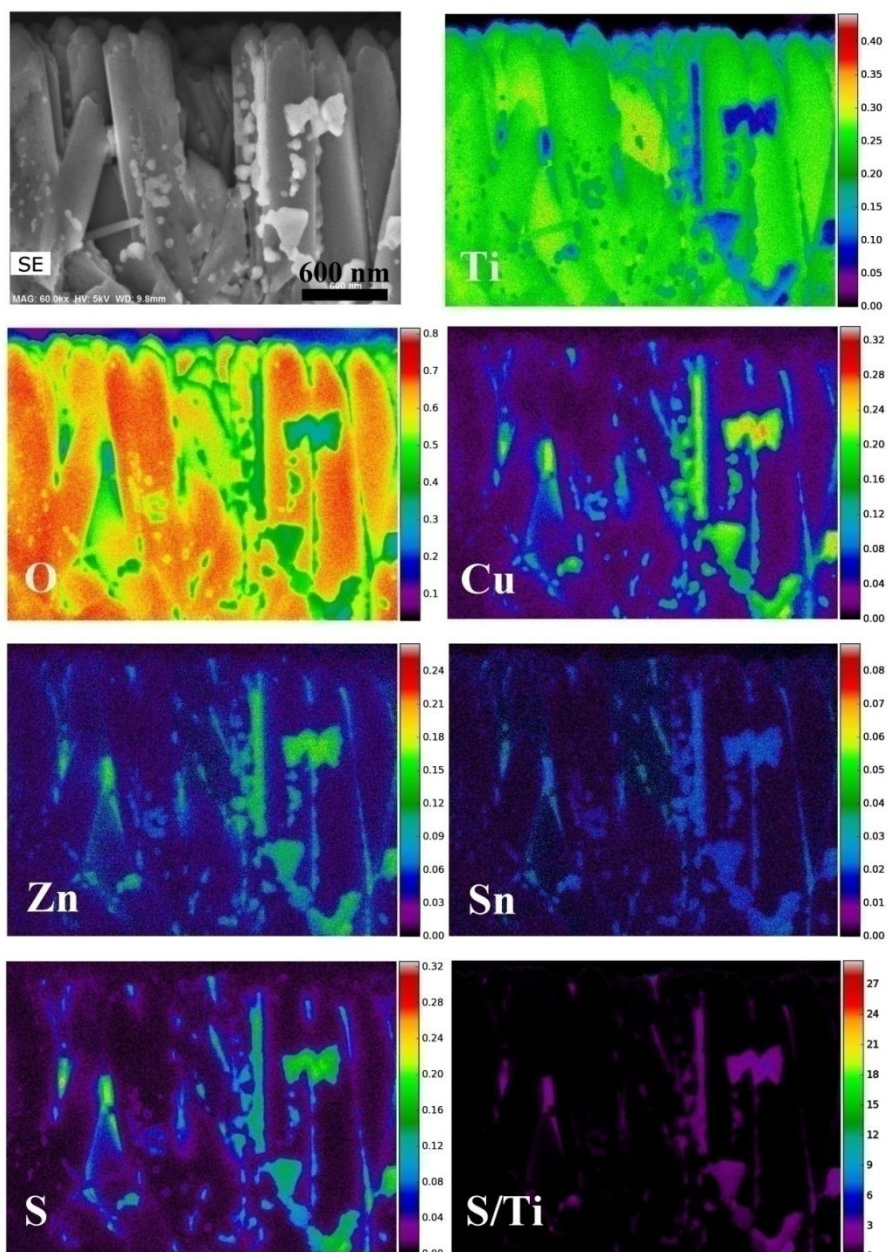


Fig. S5 EDS f-ratio maps of all individual elements in CZTS-TNR nanostructure.

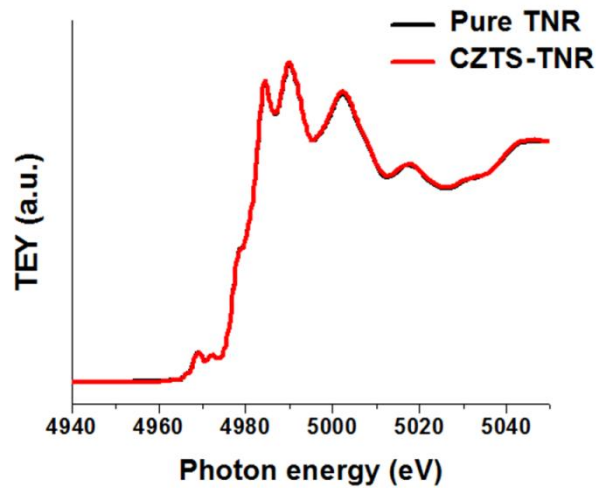


Fig. S6 Ti Normalized K-edge XANES of TNR before (black) and after (red) applying CZTS.

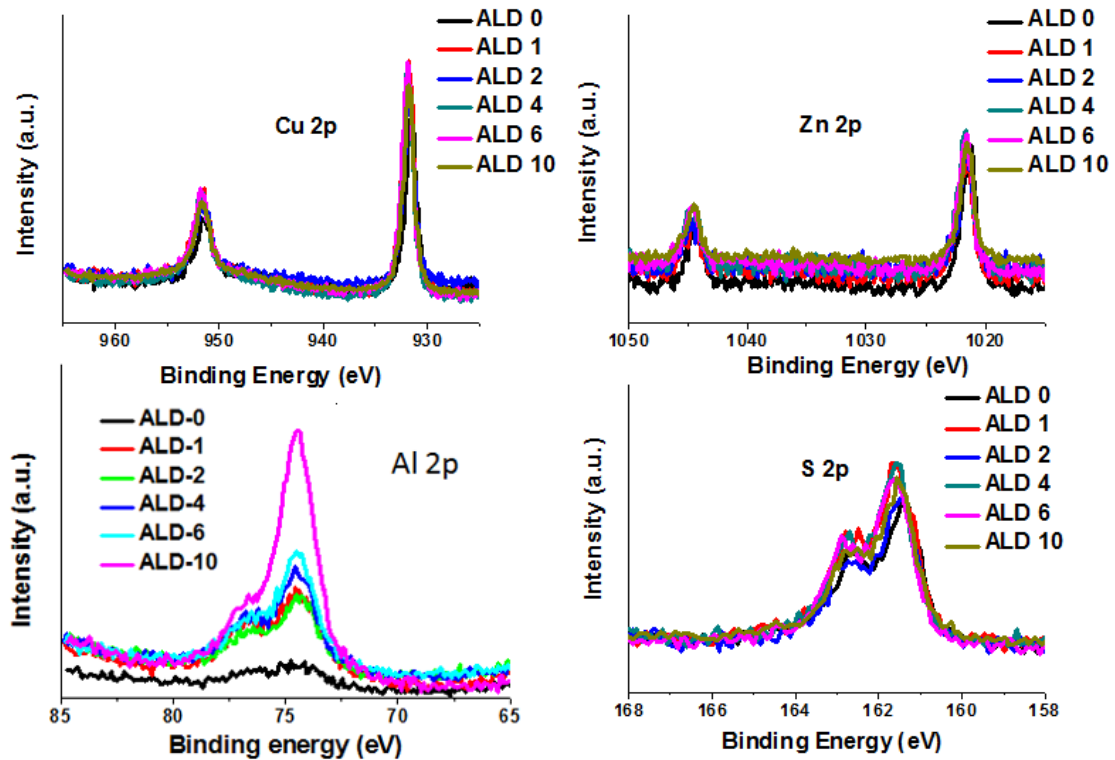


Fig. S7 XPS core line spectra of Cu, Zn, Sn and S of CZTS-Al₂O₃-TNR films prepared with different number of ALD Al₂O₃ deposition cycles.

Annealing Induced Sn Formation on TiO₂ and its Effect on Photovoltaic Property

ALD Al₂O₃ has been proven to be effective in preventing accumulation of excess Sn, herein in this supplementary section we will answer the questions of how Sn or SnO₂ was accumulated in the first place and how ALD Al₂O₃ was able to prevent Sn from being incorporated.

Firstly we tried to figure out how Sn or SnO₂ was accumulated. In our previous study, excess

amount of Sn in the form of SnO₂ was thought to be due to the oxidation of CZTS during annealing.³ However, the amount of Sn on the surface of CZTS-TiO₂ was too much in excess (almost twice of Cu) and, moreover, the Sn reduction due to predeposited Al₂O₃ (Fig. 6) is difficult to be explained solely by surface oxidation since CZTS was applied afterwards. Therefore, in order to find a proper explanation, an additional experiment was performed by placing the films of pure TiO₂ nanorods (TNR) in the furnace for annealing under the same environment as for CZTS (100 mg of Sn powder and 50 mg of S powder in Ar at 600 °C for 30 min). This was done to verify if the high temperature annealing could have any effect on rutile TiO₂ itself. Two groups of TNR substrates –one with and the other without pre-sintering in air at 500 °C–were investigated and named “TNR-A” and “TNR-NA”, respectively. These TNR substrates were then annealed in the presence of Sn and S and labeled respectively, “TNR-A-Sn-S” and “TNR-NA-Sn-S”. Fig. S8 shows the photograph of the four substrates where we see the significant colour change of TNR-NA after being annealed at inert atmosphere with Sn and S (TNR-NA-Sn-S). The change of TNR-A after further annealing (TNR-A-Sn-S) is less significant but still noticeable.

TNR-NA: Non-annealed TiO₂ nanorods

TNR-A: 500°C annealed TiO₂ nanorods

TNR-NA-Sn-S: Non-annealed TNR being annealed under Sn,S environment

TNR-A-Sn-S: 500°C annealed TNR being annealed under Sn,S environment

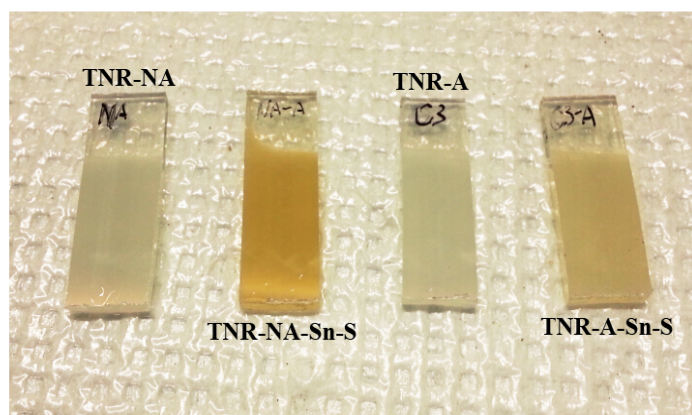


Fig. S8 Photograph of TNR substrates before annealing and after annealing under different conditions.

In order to understand this change, we started with XPS to characterize the surface of all four

substrates. Even though we do not have any coating solution that contains Sn, as it can be deduced from Fig. S9a&b, we do observe significant amount of Sn after annealing of the pure TiO₂ nanorods! The only possible source of the excess Sn must be from the Sn powder inside the furnace. In contrast, there is no evidence of sulfur residual on TNR. Then we extracted the atomic composition information from the XPS spectra and prepared the plots shown in Fig. S8c and d. As it can be seen, excess oxygen is found together with tin for TNR-NA-Sn-S and TNR-A-Sn-S, and the ratio of excess O/Sn is calculated to be ~ 2.4 giving a near SnO₂ stoichiometry. Therefore, the formed SnO₂ on the surface of CZTS-TNR must originate from the tin powder used for assisting the annealing of CZTS.

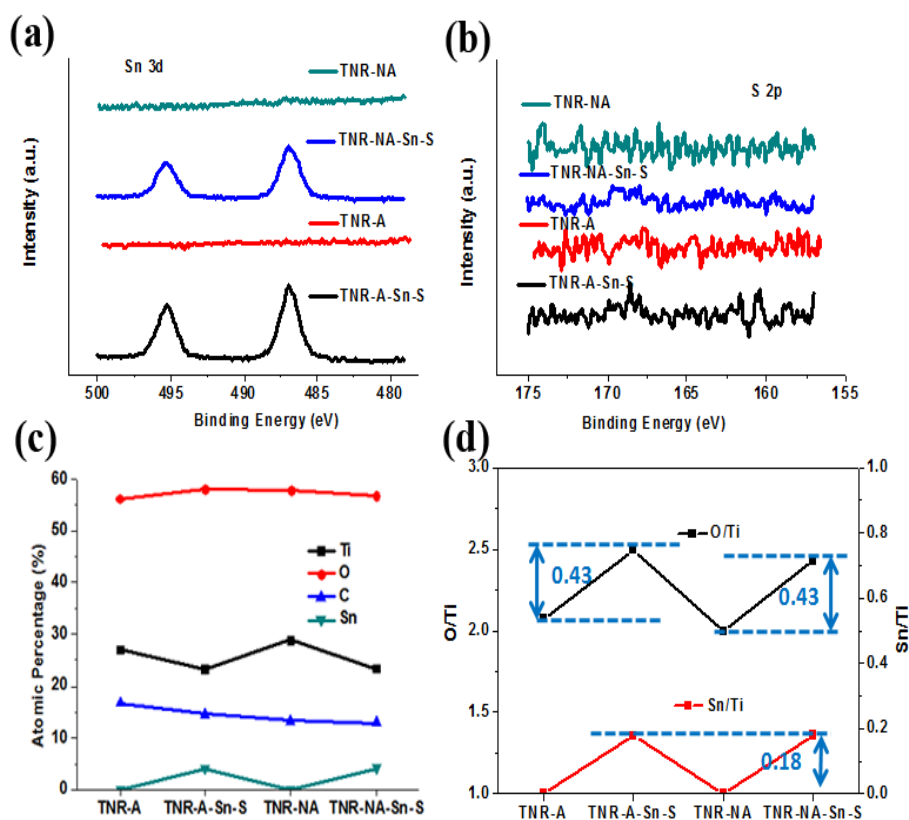


Fig. S9 XPS high resolution spectra of (a) tin and (b) sulfur of TNR substrates subjected to different annealing regimes; (c) XPS quantitative analysis and (d) converted O/Ti and Sn/Ti ratios.

To understand more about this Sn selective incorporating phenomenon, we performed optical characterization tests. Fig. S10a shows a comparison of the light absorption spectra among all the four TNR samples together with CZTS-TNR. It is clear that CZTS-TNR has the best visible light absorbing property of all. TNR-NA-Sn-S shows apparent visible light absorbing property which

agrees with its colour. TNR-A-Sn-S can also absorb visible light but to a less extent while the TNR-A and TNR-NA only absorb UV light. To estimate the bandgap, the absorption coefficient was calculated using the equation $\alpha = -\ln[T/(1-R)]/d^5$, where T is the transmittance, R is the reflectance, and d is the film thickness, which in our case is $\sim 1.5 \mu\text{m}$. Then by applying the Tauc plot of $(h\nu\alpha)^2$ versus $h\nu$ as shown in Fig. S10b,^{6,7} the bandgap of TNR-A and TNR-NA is determined to be $\sim 3.1\text{eV}$, which practically matches that of the pure rutile phase. In comparison, the absorption bandgap has been narrowed after annealing in a Sn/S environment ($\sim 2.95\text{eV}$ for TNR-A-Sn-S and $\sim 2.83\text{eV}$ for TNR-NA-Sn-S). Therefore, the incorporation of excess Sn has modified the optical property of rutile. It appears in other words that the high temperature Sn doping has induced an intermediate energy state into TiO_2 ^{8,9}.

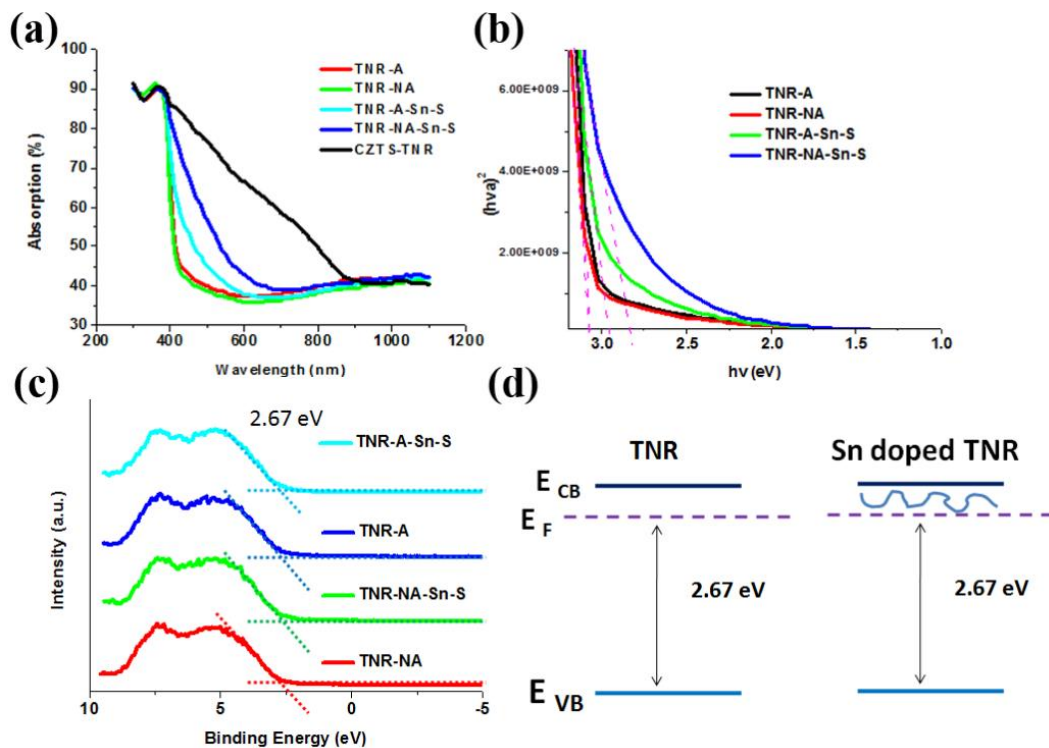


Fig. S10 (a) Light absorption spectra of CZTS-TNR and TNR substrates subjected to different annealing protocols and (b) converted curves for bandgap estimation; (c) valence spectra of TNR substrates subjected to different annealing regimes and (d) schematic band diagrams of the TNR before and after tin doping.

To see if the doping of TiO_2 with Sn have any effect on its electronic property, these four TNR

films were assembled into photoelectrochemical cells without CZTS.² Their photovoltaic performance is shown in Fig. S11. As it becomes evident Sn doping had a negative impact on TNR; the same data also show that performing annealing the TNR prior to annealing with Sn/S helps preserve somewhat the electronic property of TiO₂. Comparing to the optical characteristics in Fig. S10a and b, Fig. S11b does not show the corresponding broadening of EQE responses, meaning that this enhanced visible light absorption is ineffective in terms of the photoelectron generation/collection. Judging from the significant V_{oc} drop, the Sn doped energy state is likely to have enhanced charge recombination hence lowering the electron conducting ability of TiO₂. To estimate the possible position of the doping energy level, the XPS valence spectra were taken as shown in Fig. S10c. By fitting these spectra we determined the valence band position referring to the Fermi level to be 2.67 eV for all samples; no additional defect state could be identified in between, which means the Sn doping state if there were any must be existed near the conduction band as illustrated in Fig. S9d. In fact, this finding agrees with reported computational results that Sn doping in rutile lowers the conduction band bottom.¹⁰ It was reported that Sn doping is favorable when it is in the form of Ti atom being substituted,^{8, 11, 12} which appears to be the case with our results as derived from the additional Sn/O ratio of ~2.4 (similar ratio of pure TiO₂) in Fig. S9d. We attempted to curtail the problem of tin doping by removing it during annealing of CZTS-TNR films. However, this approach did not work as again we found excess Sn/O of ~2.4, this time the Sn doped into TNR originating from CZTS itself. But this problem of Sn doping was minimized upon ALD deposition of Al₂O₃ on TNR before the deposition of CZTS.

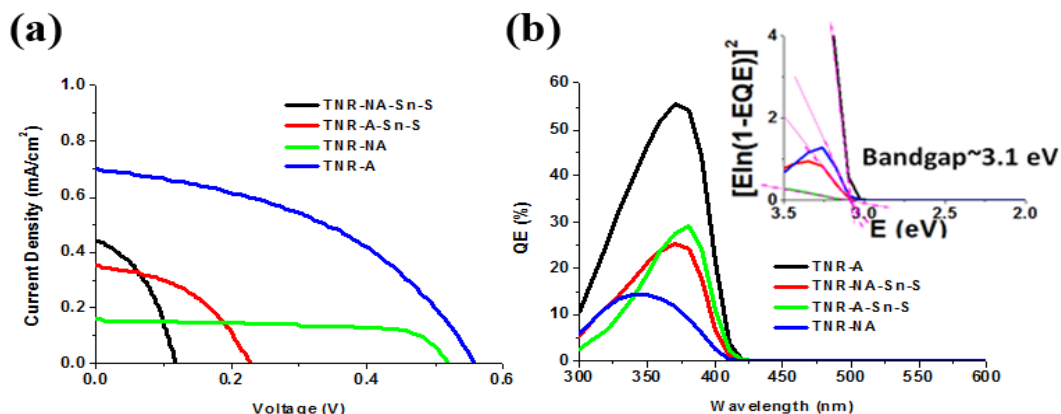


Fig. S11 (a) J-V characteristics and (b) IPCE spectra of TNR substrates subjected to different annealing regimes; inset shows the bandgap calculation from IPCE.

Effect of ALD Al_2O_3 on the Formation of SnO_2

We have already proven that ALD coating of Al_2O_3 is beneficial in reducing Sn doping into TNR and prolonging the electron lifetime for the optoelectronic devices. Now we are prepared to answer the second question- how Al_2O_3 was able to prevent Sn doping. Annealing under Sn/S environment was again performed but on ALD TNR films without the interference of CZTS, and the deposition cycles were varied from 0~10 (noted as 0~10 c). Fig. S12 shows the XPS core-line spectra of Ti 2p, S 2p, Al 2p and Sn 3d, where we find the apparent peak intensity to decrease for both Ti and Sn as the number of ALD cycles (peak intensity increase of Al) increases. The reduction of Ti signal is due to the shallower XPS detection depth of TiO_2 as the Al_2O_3 coating becomes thicker (increased number of ALD cycles). The trend of Sn peak area change with increased ALD cycle is plotted in Fig. S13a. The atomic ratio of Sn/Ti is plotted in Fig. S13c. Although there is a sharp decline of both Ti and Sn content after Al_2O_3 deposition, the value of Sn/Ti is consistent with and without Al_2O_3 . Therefore, it is reasonable to say that SnO_2 only forms on TiO_2 surface and since the predeposited Al_2O_3 “islands” contributes to reducing the exposed area of TiO_2 , the total amount of incorporated Sn is reduced. The schematic depiction in Fig. 6d helps to better understand this Al_2O_3 coating effect. Although current ALD technique has been proven to be able to reduce Sn content, it would be more effective if a continuous ultrathin layer of Al_2O_3 coating instead of “nanoislands” could be realized.

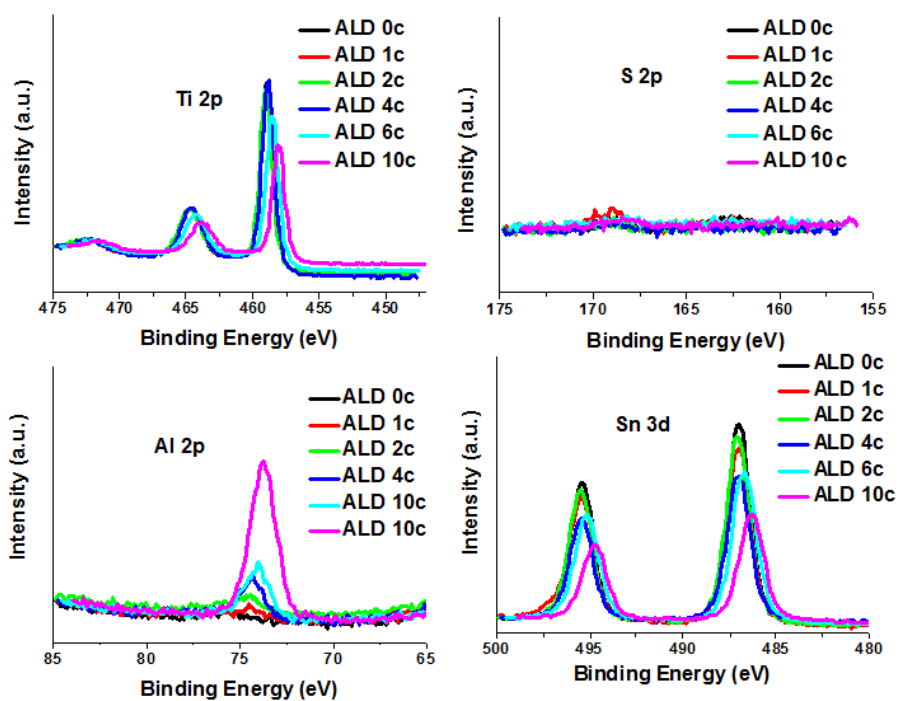


Fig. S12 XPS core line spectra of Ti, S, Al and Sn of TNR- Al_2O_3 films prepared with different number of ALD Al_2O_3 cycles.

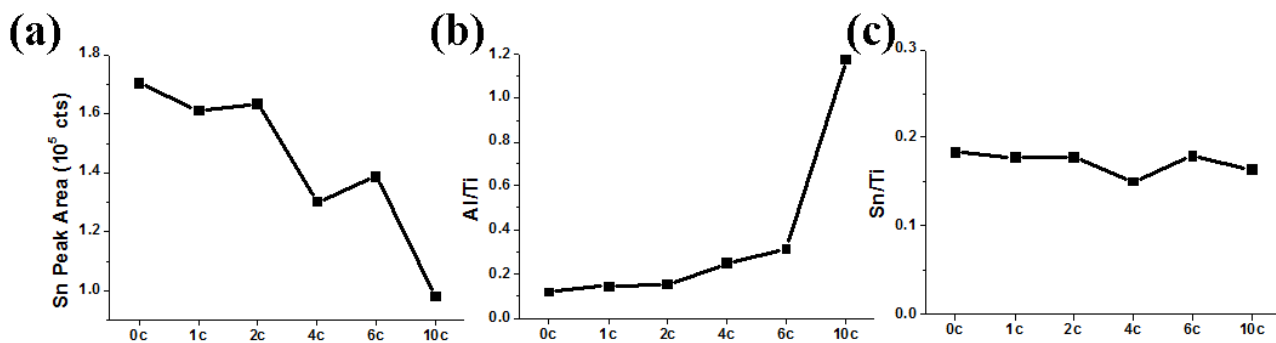


Fig. S13 (a) The absolute Sn 2p peak area, b) atomic ratio of Al/Ti and c) Sn/Ti atomic ratio of TNR- Al_2O_3 films.

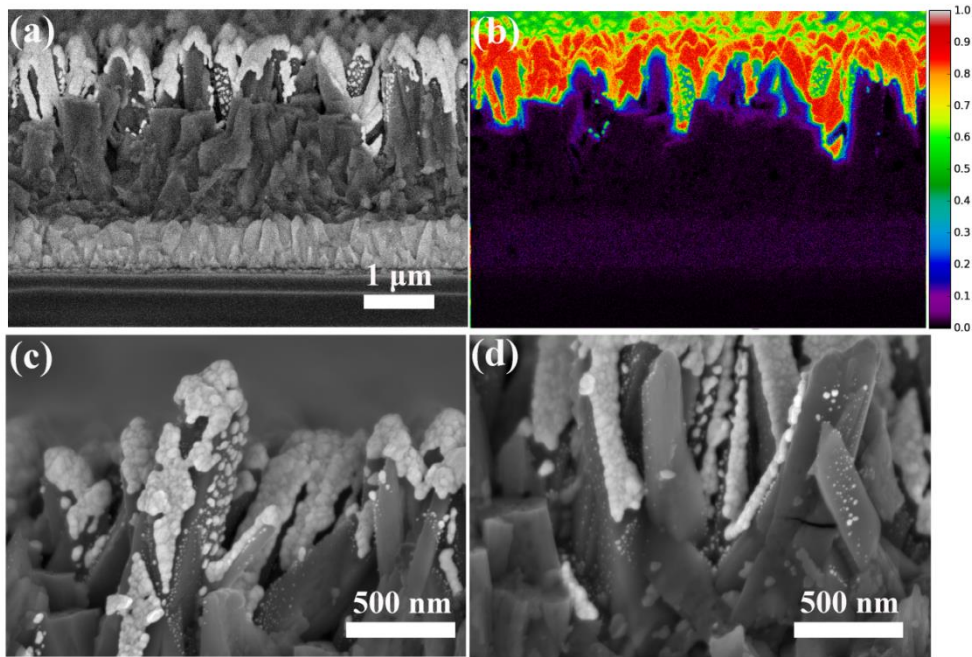


Fig. S14 (a, c, d) SEM images of TNR-Al₂O₃-CZTS-Au film cross section and (b) EDS map of Au.

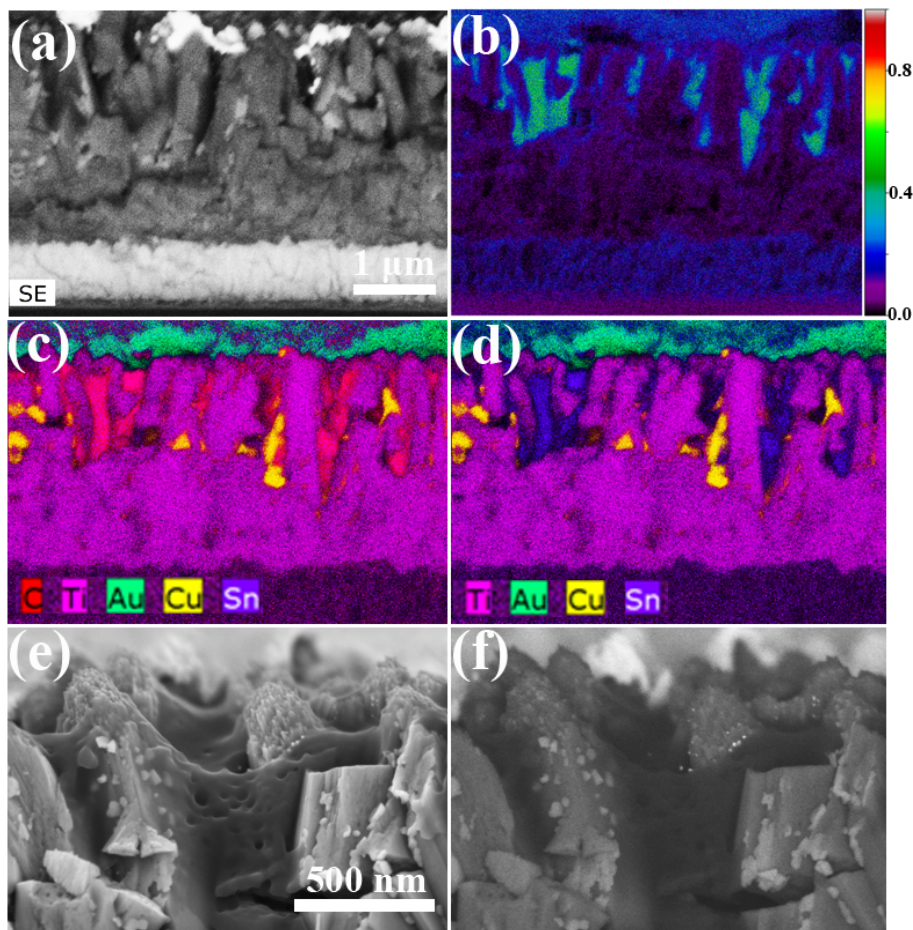


Fig. S15 (a) SEM secondary electron (SE) image and (b) EDS f-ratio map of carbon; and mixed maps of the TNR-CZTS-spiro-OMeTAD-Au device with (c) and without (d) labelling carbon (C); (e) higher magnification SE and (f) BSE image of the spiro-OMeTAD coated CZTS-TNR film.

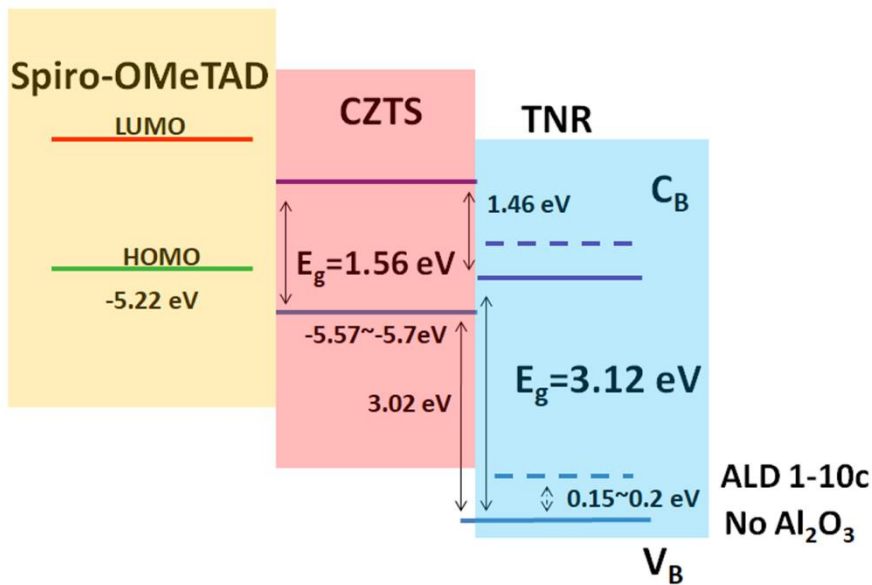


Fig. S16 Energy level diagram of CZTS- TNR-CZTS-spiro-OMeTAD.¹³⁻¹⁶ The VB energy of CZTS is obtained from ref.13&14, the HOMO level of spiro-OMeTAD is from ref.15&16

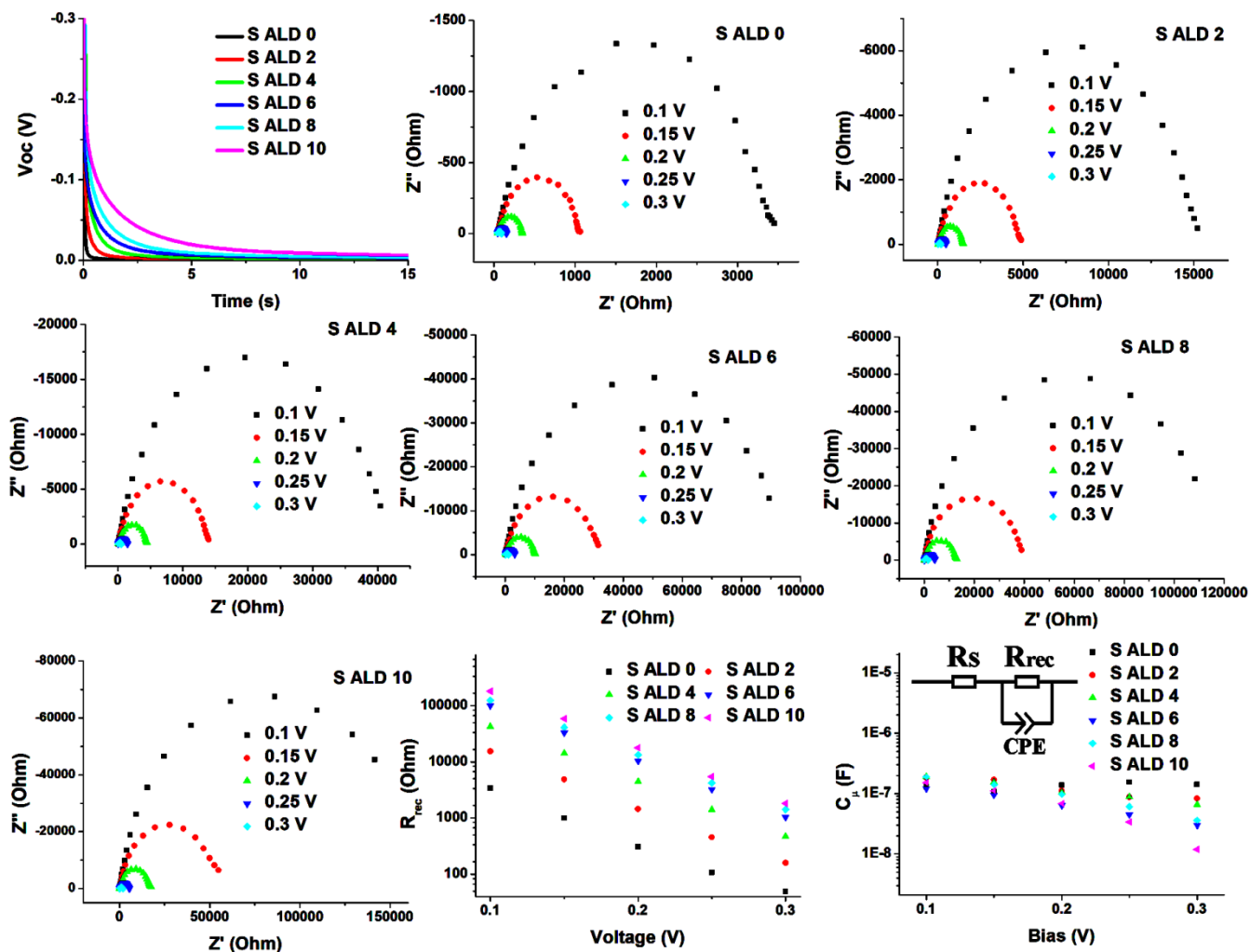


Fig. S17 OCVD and EIS measurements of CZTS-TNR-Spiro-OMeTAD devices with different Al₂O₃ layers and the extracted charge recombination resistance (R_{rec}), equivalent chemical

capacitance (C_{μ}); inset of the last chart shows the equivalent circuit used for EIS fitting.

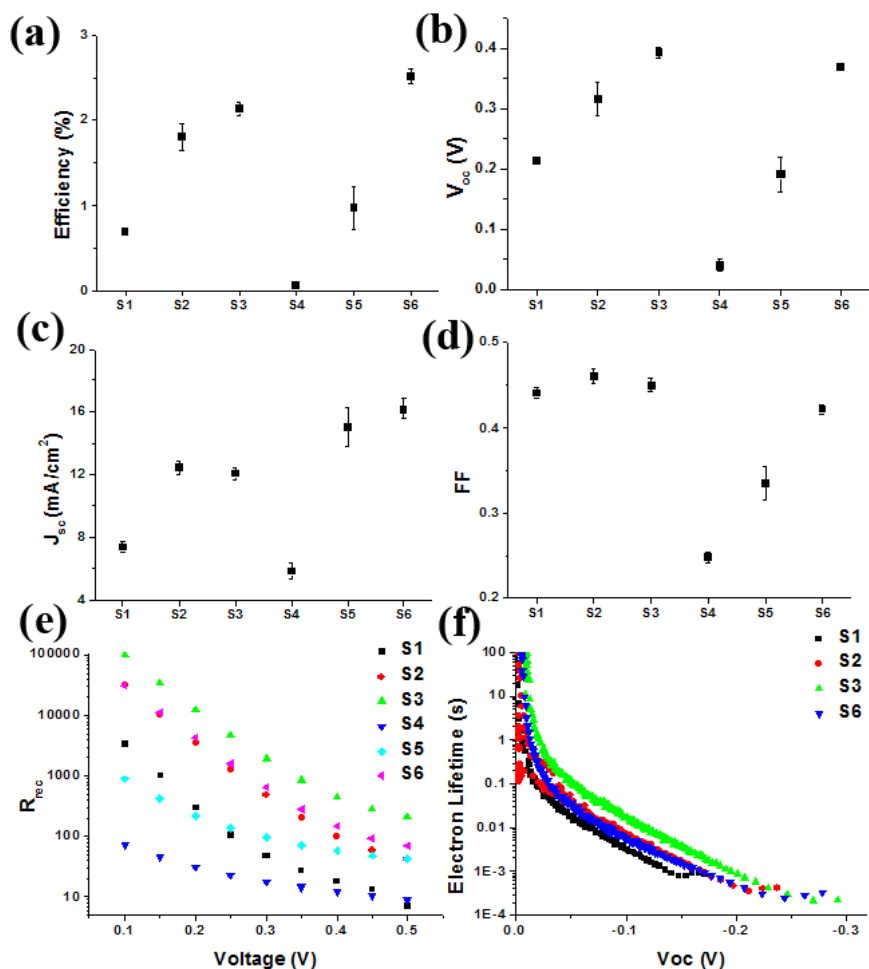


Fig. S18 (a-d) Photovoltaic performance of devices S1-S6 with error bars; (e) EIS-measured recombination resistance and (f) OCVD-measured electron lifetime.

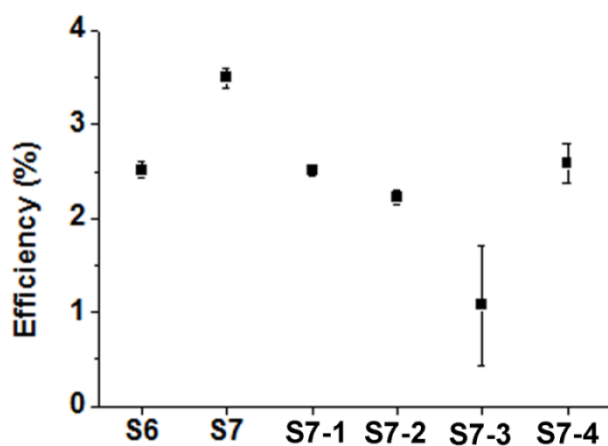


Fig. S19 Efficiency of devices with TNR films grown under different conditions (see Table S1).

Table S1. Synthesis conditions of different TNR films and the average efficiency of respective fabricated devices.

Film ID	Titanium Butoxide	HCl Aqueous Solution	Reaction Temperature	Reaction Time	Average Efficiency (%)
S6	0.75 M	18 %	150 °C	6 h	2.5
S7	0.5 M	18 %	150 °C	10 h	3.5
S7-1	0.75 M	18 %	150 °C	3 h	2.5
S7-2	0.75 M	18 %	150 °C	10 h	2.2
S7-3	0.5 M	18 %	150 °C	3 h	1.1
S7-4	0.5 M	18 %	150 °C	6 h	2.6

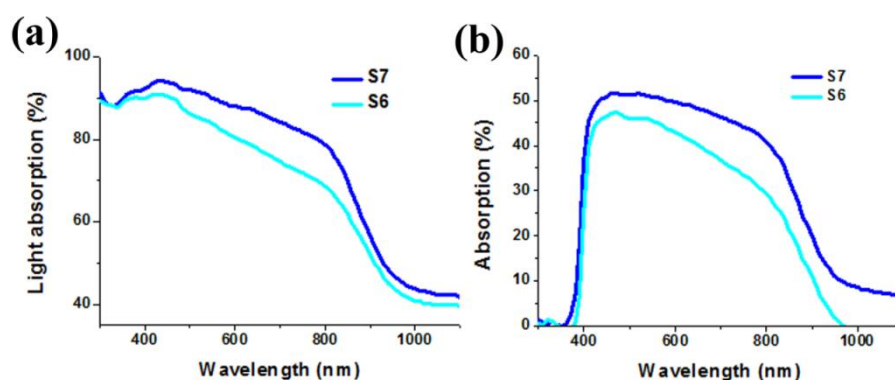


Fig. S20 Light absorption of S6 and S7 photoelectrodes: (a) before and (b) after deducting the contribution of TNR.

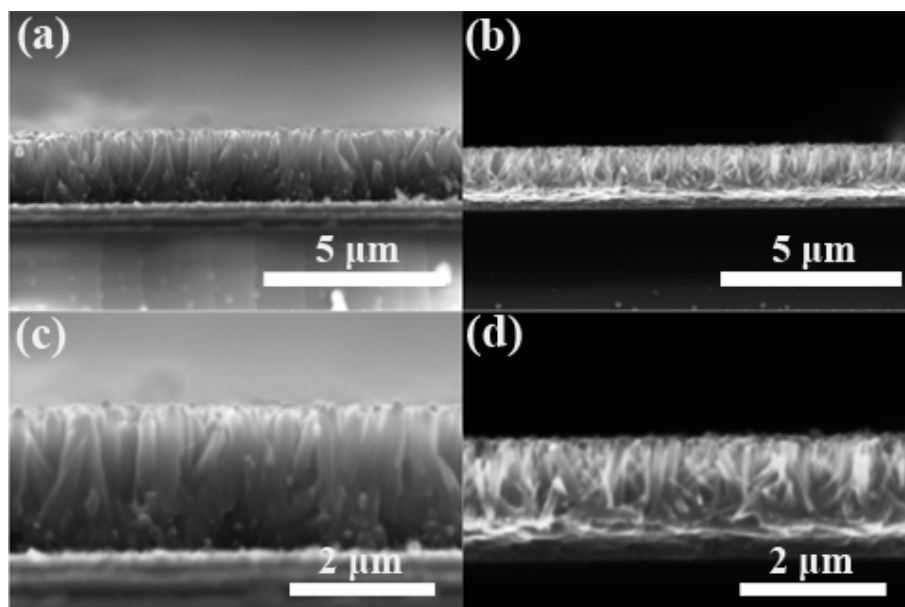


Fig. S21 Cross sectional SEM images of TNR for S6 (a, c) and S7 (b, d) films.

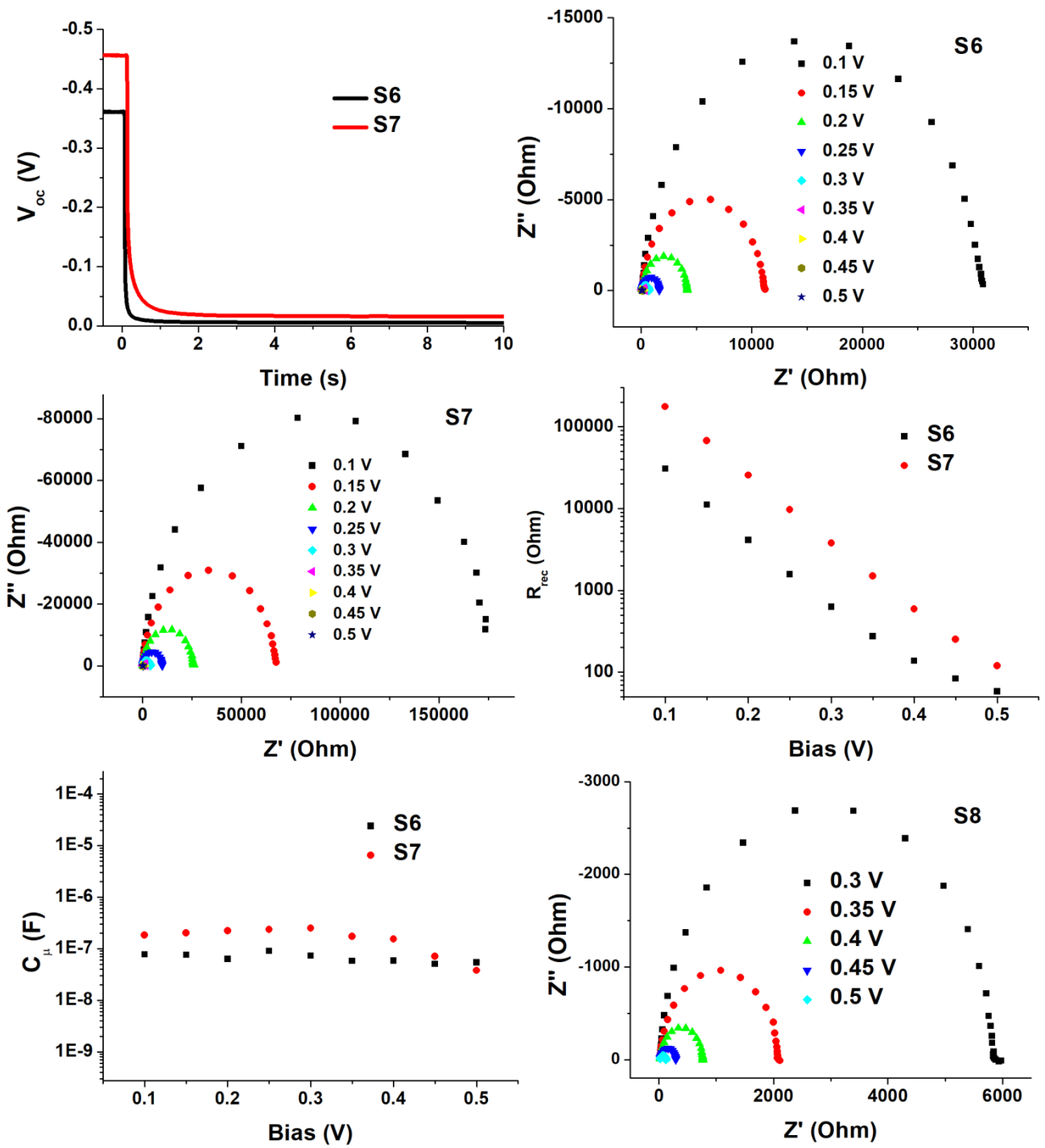


Fig. S22 OCVD and EIS measurements of S6, S7 and S8 devices and the extracted charge recombination resistance (R_{rec}), equivalent chemical capacitance (C_{μ}) of S6 and S7.

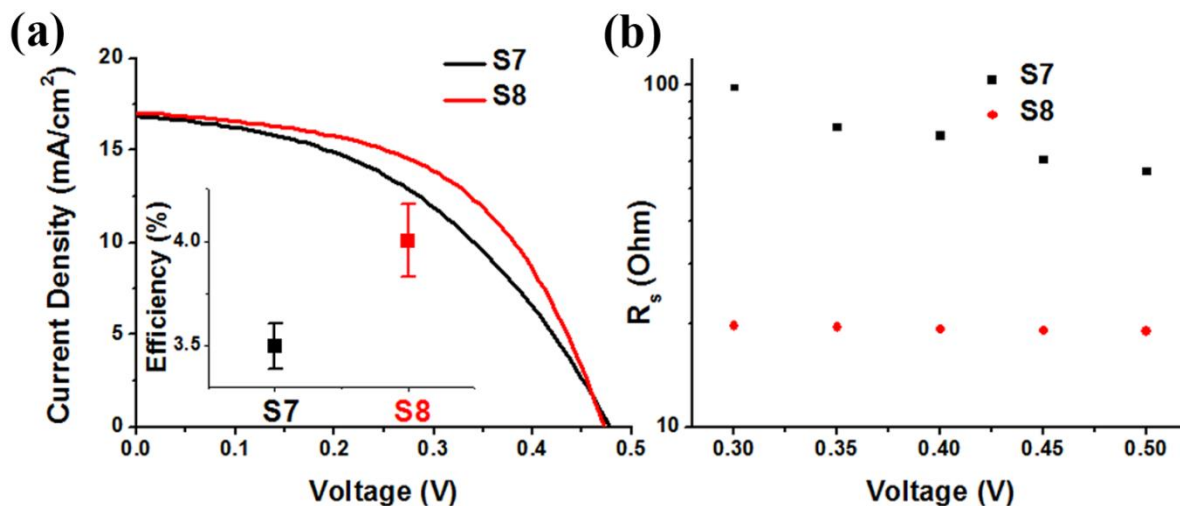


Fig. S23 (a) J-V and (b) series-resistance extracted from EIS measurement of devices S7 and S8. Inset of (a) shows the measured average efficiency and standard deviation of 8 S7 and S8 devices.

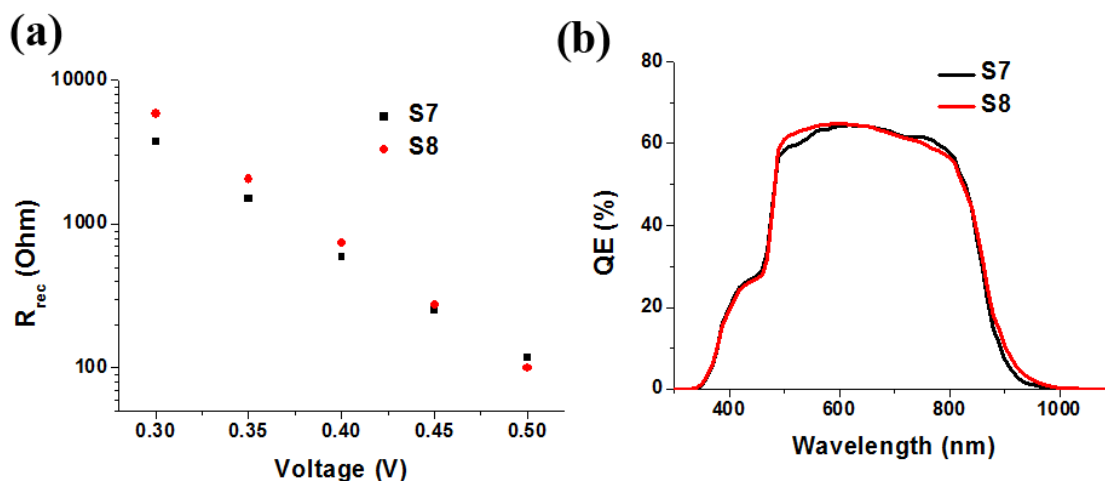


Fig. S24. (a) Recombination resistance (extracted from EIS) and (b) EQE of devices S7 and S8 (see Table S1).

References:

1. B. Liu and E. S. Aydil, *J. Am. Chem. Soc.* 2009, **131**, 3985-3990.
2. Z. Wang, S. Ran, B. Liu, D. Chen and G. Shen, *Nanoscale*, 2012, **4**, 3350-3358.
3. Z. Wang, R. Gauvin and G. Demopoulos, *Nanoscale*, 2017, **9**, 7650-7665.
4. M. A. Contreras, M. J. Romero, B. To, F. Hasoon, R. Noufi, S. Ward and K. Ramanathan, *Thin Solid Films*, 2002, **403**, 204-211.
5. E. Thimsen, S. C. Riha, S. V. Baryshev, A. B. F. Martinson, J. W. Elam and M. J. Pellin, *Chem. Mater.*, 2012, **24**, 3188-3196.

6. D. Tiwari, T. K. Chaudhuri, A. Ray and K. D. Tiwari, *Thin Solid Films*, 2014, **551**, 42-45.
7. A. B. Murphy, *Sol. Energy Mater. Sol. Cells*, 2007, **91**, 1326-1337.
8. F. E. Oropeza, B. Davies, R. G. Palgrave and R. G. Egdell, *Phys. Chem. Chem. Phys.*, 2011, **13**, 7882-7891;
9. F. Wang, J. H. Ho, Y. Jiang and R. Amal, *Acs Appl. Mater. Interfaces*, 2015, **7**, 23941-23948.
10. X. Yu, C. Li, H. Tang, Y. Ling, T. A. Tang, Q. Wu and J. Kong, *Comp. Mater. Sci.*, 2010, **49**, 430-434.
11. F. R. Sensato, R. Custodio, E. Longo, A. Beltran and J. Andres, *Catal. Today*, 2003, **85**, 145-152;
12. M. H. Harunsani, F. E. Oropeza, R. G. Palgrave and R. G. Egdell, *Chem. Mater.*, 2010, **22**, 1551-1558.
13. R. Rajeswari, M. Mrinalini, S. Prasanthkumar and L. Giribabu, *Chem. Rec.* 2017, **17**, 681-699;
14. Y. Wang, C. X. Li, X. J. Yin, H. Wang and H. Gong, *Ecs J. Solid State Sci.*, 2013, **2**, Q95-Q98.
15. H. Zhou, Q. Chen, G. Li, S. Luo, T. Song, H. S. Duan, Z. Hong, J. You, Y. Liu and Y. Yang, *Science*, 2014, **345**, 542-546.
16. J. Burschka, A. Dualeh, F. Kessler, E. Baranoff, N. Cevey-Ha, C. Yi, M. K. Nazeeruddin and M. Grätzel, *J. Am. Chem. Soc.*, 2011, **133**, 18042-18045.